

# Investigation of the Birdcage-like Coil for Active Magnetic Shielding

Christopher M. Loftson

Undergraduate Honours Thesis

Advisor: Dr. Chris Bidinosti

University of Winnipeg

Winnipeg, MB Canada

May 10, 2013

## Abstract

The birdcage-like coil, composed of independent saddle coils bound to the surface of a cylinder, approximates the infinite cylindrical surface current  $K \sin(n\phi)\hat{z}$ . Research was geared toward the applicability of the birdcage-like coil as a possible active magnetic shield for use in measuring the neutron electric dipole moment. This coil produces a transverse magnetic field with good homogeneity. A prototype coil was built and field mapped for homogeneity. A computer model of the birdcage-like coil was used to investigate its properties. A numerical search in parameter space was conducted to find a set of parameters in order to design a coil with better homogeneity.

# Contents

<b>1</b>	<b>Introduction</b>	<b>1</b>
<b>2</b>	<b>Theory</b>	<b>2</b>
2.1	The infinitely long ideal surface current . . . . .	2
2.2	The birdcage-like coil and its current configuration . . . . .	5
2.3	Contour plots of the birdcage-like model magnetic field . . . . .	12
<b>3</b>	<b>Prototype design and characterization</b>	<b>13</b>
3.1	Features of the birdcage-like coil . . . . .	13
3.2	Prototype construction . . . . .	15
3.3	Methods . . . . .	17
3.3.1	Self-resonance measurement . . . . .	17
3.3.2	Resistance and inductance measurements . . . . .	18
3.3.3	Field mapping along the $x$ - and $y$ -axes . . . . .	20
<b>4</b>	<b>Results</b>	<b>21</b>
4.1	Prototype self-resonance, resistance, and inductance . . . . .	22
4.2	Field mapping . . . . .	23
4.3	End current discretization . . . . .	27
4.4	Searching for optimum parameters . . . . .	30
4.5	Comparing the birdcage-like coil to the square Helmholtz coil . . . . .	32
<b>5</b>	<b>Discussion</b>	<b>34</b>
5.1	Future directions . . . . .	36
<b>6</b>	<b>Conclusion</b>	<b>37</b>
<b>A</b>	<b>Supplementary equations for the ideal <math>B</math> field</b>	<b>39</b>



## List of Tables

1	Some specifications of the prototype birdcage-like coil . . . . .	16
2	Prototype self-resonance . . . . .	22
3	Prototype resistance and inductance per segment . . . . .	22
4	Prototype parameters . . . . .	25
5	Homogeneity of prototype field along transverse axes . . . . .	27

# List of Figures

1	The $\sin(n\phi)$ field line diagram . . . . .	4
2	The $\cos(n\phi)$ field line diagram . . . . .	5
3	The birdcage-like coil . . . . .	6
4	A diagrammatic representation of birdcage-like approximation of $\sin(n\phi)$ and $\cos(n\phi)$ . . . . .	8
5	A segment current diagram . . . . .	9
6	Magnetic field contour plots in the $z = 0$ plane . . . . .	14
7	The prototype coil constructed for testing . . . . .	15
8	Circuit diagram for the self-resonance measurement . . . . .	18
9	Circuit diagram for the resistance and inductance measurement . . . . .	19
10	Diagram of the apparatus used for field mapping the prototype coil . . . . .	21
11	Prototype field data along $x$ - and $y$ -axis . . . . .	24
12	Prototype coil spacing between segments . . . . .	26
13	The straight end current coil . . . . .	27
14	Convergence of $\mathbf{B}$ as end segment approximation improves . . . . .	28
15	Parameter space search for optimum parameters . . . . .	31
16	Contour plots of both the square Helmholtz coil and the birdcage-like coil . . . . .	33
17	A continuous function approximated by discrete line segments . . . . .	40

# 1 Introduction

For certain applications in experimental physics, it is desirable to maintain a magnetic field in some region of interest that is homogeneous and constant in time. However, the magnetic field in laboratories is not usually homogeneous nor constant in time. This raises the question, what can be done to counteract any fluctuations in a magnetic field over space and time?

One method to cancel out fluctuations is to use active magnetic shielding. First, a homogeneous magnetic field is generated within a region of interest. Second, this magnetic field must be manipulated in real-time to counteract any fluctuations due to any outside source. The magnetic field will then be kept unchanged over space and time in that region. Active magnetic shielding is named active because of this real-time counteraction to keep the field constant in time. If the magnetic field can be made homogeneous and it counteracts changes in time, we have total control over the field in a specified region. Then, any experiment dependant on a precise measurement or manipulation of the magnetic field can be conducted as desired.

One example of an experiment where a very homogeneous and steady field is necessary is the measurement of the neutron electric dipole moment (nEDM). The nEDM has not yet been measured to be non-zero. If the nEDM is non-zero, it would be incredibly weak, and therefore difficult to detect. A large constraint to the measurement of the nEDM is the homogeneity and constancy of the magnetic field within the region that the experiment takes place. If one hopes to measure the nEDM precisely, control over the magnetic field in a region is necessary.

The Biot-Savart law tells us that a steady current gives rise to a magnetic field  $\mathbf{B}$  that is constant in time. Steady currents arranged in the proper way will create a homogeneous field within a certain region. However, it is not sufficient to be able to produce a homogeneous field. One also needs to be able to manipulate the current distribution in such a way as to change the direction of the homogeneous field. One way to manipulate a current distribution for such a task would be to change the magnitude of different currents that make up the

distribution. It is also valuable for background gradient fields to be cancelled with this current structure thereby giving even more homogeneity.

Even once a theoretical current distribution that can generate arbitrary homogeneous and gradient fields is found, a practical coil design must be created to either generate this current distribution or approximate it. The purpose of this paper is to investigate the birdcage-like coil design which approximates an ideal current distribution. The ideal current distribution itself generates a homogeneous field and gradient fields in arbitrary direction. This particular coil design may be appropriate for use as an active magnetic shield.

A prototype birdcage-like coil was built and tested for homogeneity. It was also tested to see whether it could generate a  $\mathbf{B}$  field in some predicted direction. If the birdcage-like coil is shown to produce homogeneity in a specified region and it can control field direction, the coil will have some functionality as an active magnetic shield.

Computer modeling of this coil design and its magnetic field was studied as well. End current discretization and ideal coil parameters were investigated using modeling for the purpose of future design ideas. Also, the homogeneity of the birdcage-like coil's field was compared to the field of the square Helmholtz coil. This paper will also put forward results of the computer modeling.

## 2 Theory

To begin I will discuss a current distribution that gives rise to a uniform field and to gradient fields. We will look at currents bound to the surface of a cylinder, which make for simple coil construction and winding. Therefore, I will first discuss cylindrical surface currents.

### 2.1 The infinitely long ideal surface current

An infinitely long cylindrical surface current of  $\mathbf{K} = K \sin(n\phi)\hat{\mathbf{z}}$  will give rise to either a transverse uniform field for  $n = 1$ , or transverse gradient fields for  $n > 1$ , in the region within

the coil. It cannot, however, generate a field pointing along its axial direction. An axial field must be left up to a separate coil to generate. Here  $K$  is constant current-per-unit-length, and the mode  $n$  is a positive integer. Also,  $(\rho, \phi, z)$  are the usual cylindrical coordinates. To see that such a current distribution gives rise to uniform and gradient fields, we start with the vector potential due to this current distribution, derived elsewhere [1, 2]:

$$\mathbf{A}(\rho, \phi) = \frac{\mu_0 a K \sin(n\phi)}{2n} \hat{\mathbf{z}} \left(\frac{\rho}{a}\right)^n, \quad \rho < a. \quad (1)$$

Here  $a$  is the radius of the cylinder.

Taking the curl of  $\mathbf{A}$ , we obtain an expression for the field  $\mathbf{B}$  in the region  $\rho < a$ :

$$\mathbf{B}(\rho, \phi) = \frac{-\mu_0 K}{2} \left(\frac{\rho}{a}\right)^{n-1} [\sin(n\phi) \hat{\boldsymbol{\phi}} - \cos(n\phi) \hat{\boldsymbol{\rho}}]. \quad (2)$$

Transforming into cartesian unit vectors we get,

$$\mathbf{B}(\rho, \phi) = \frac{-\mu_0 K}{2} \left(\frac{\rho}{a}\right)^{n-1} [-\cos((n-1)\phi) \hat{\mathbf{x}} + \sin((n-1)\phi) \hat{\mathbf{y}}], \quad \rho < a, \quad (3)$$

where,

$$\rho = \sqrt{x^2 + y^2} \quad \phi = \tan^{-1}\left(\frac{y}{x}\right)$$

$$\hat{\boldsymbol{\rho}} = \cos(\phi) \hat{\mathbf{x}} + \sin(\phi) \hat{\mathbf{y}} \quad \hat{\boldsymbol{\phi}} = -\sin(\phi) \hat{\mathbf{x}} + \cos(\phi) \hat{\mathbf{y}}.$$

In Equation 3, it is easy to see that  $\mathbf{B}$  describes uniform and gradient fields for  $n = 1$  and  $n > 1$ , respectively. If  $n = 1$  then  $\mathbf{B} = \mu_0 K/2 \hat{\mathbf{x}}$ , which is constant in magnitude and direction. If  $n > 1$ , and we take  $\phi = 0$  for simplicity, then  $\mathbf{B} \propto x^{n-1} \hat{\mathbf{x}}$ . Therefore, along the  $x$ -axis ( $\phi = 0$ ),  $\mathbf{B}$  describes a gradient of degree  $n - 1$ .

More generally,  $\mathbf{B}$  goes as  $\rho^{n-1}$  in any arbitrary radial direction in the transverse plane.

From Equation 2,

$$|\mathbf{B}| = \sqrt{\left(\frac{-\mu_0 K}{2} \left(\frac{\rho}{a}\right)^{n-1}\right)^2 [\cos^2((n-1)\phi) + \sin^2((n-1)\phi)]} = \frac{\mu_0 K}{2} \left(\frac{\rho}{a}\right)^{n-1}$$

$$\Rightarrow |\mathbf{B}| \propto \rho^{n-1}.$$

This applies for any value of  $\phi$ . Therefore,  $|\mathbf{B}|$  is a gradient along any  $\phi = \text{constant}$  curve.

Note that it is equally acceptable to generate transverse uniform and gradient fields for a  $\cos(n\phi)\hat{\mathbf{z}}$  surface current distribution. I have chosen to work with the  $\sin(n\phi)\hat{\mathbf{z}}$  distribution for this paper. See Appendix A for the above equations when  $\rho > a$  and when  $\mathbf{K} = K \cos(n\phi)\hat{\mathbf{z}}$ .

Figures 1 and 2 show field lines of  $\mathbf{B}$  in a transverse plane both inside and outside of the infinitely long cylinder. For each subfigure, field line density is proportional to field strength. For  $n = 1$ , field line density and direction is constant. For  $n > 1$ , field line density is decreasing as  $\rho$  increases from 0 to  $a$ .

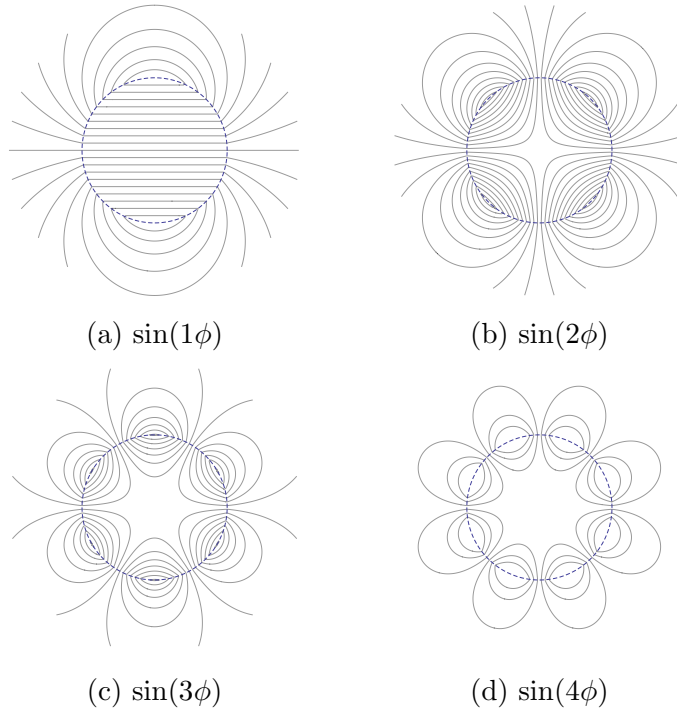


Figure 1: Magnetic field lines for the ideal  $\sin(n\phi)$  current distribution. The dashed line is the circumference of the infinitely long cylinder.

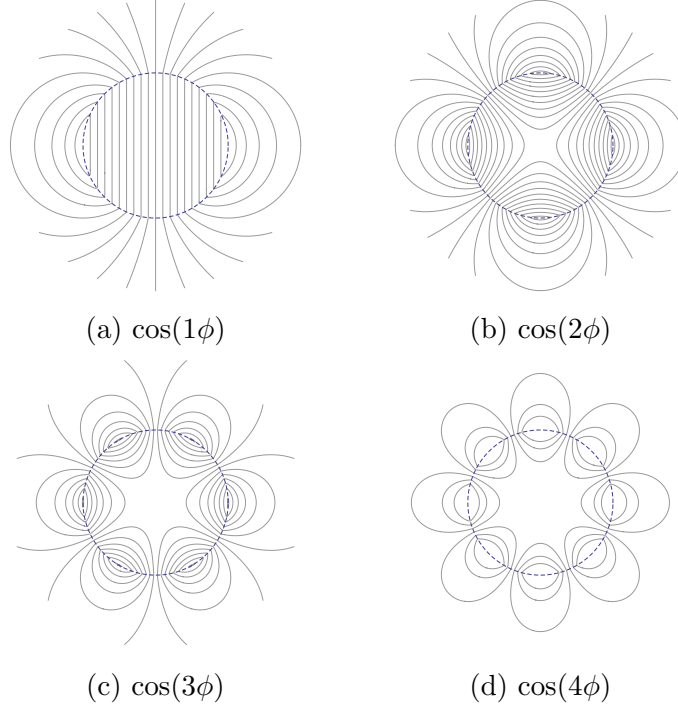


Figure 2: Magnetic field lines for the ideal  $\cos(n\phi)$  current distribution. The dashed line is the circumference of the infinitely long cylinder. Field line density is the same as in Figure 1. Note that each  $\cos(n\phi)$  field line plot is a rotation of the  $\sin(n\phi)$  field line plot of angle  $\frac{\pi}{2n}$ .

## 2.2 The birdcage-like coil and its current configuration

The birdcage-like coil is a design that approximates the ideal  $\sin(n\phi)$  surface current distribution. The birdcage-like coil does so by running appropriate axial currents at discrete evenly-spaced values of  $\phi$  along the cylindrical surface. There are an even number of saddle coils,  $N$ , hereupon referred to as segments, that cover the curved surface of a cylinder. Figure 3 depicts the birdcage-like coil. The way the birdcage-like coil works is that each segment runs current independently. The current in axial rungs of adjacent segments sum together to produce the appropriate  $\sin(n\phi)$  distribution. In theory, each segment runs current independent of the other segments. However, if two or more segments require the same current to produce a particular field, they may be run in series or in parallel to reduce the number of power supplies necessary to generate that magnetic field.

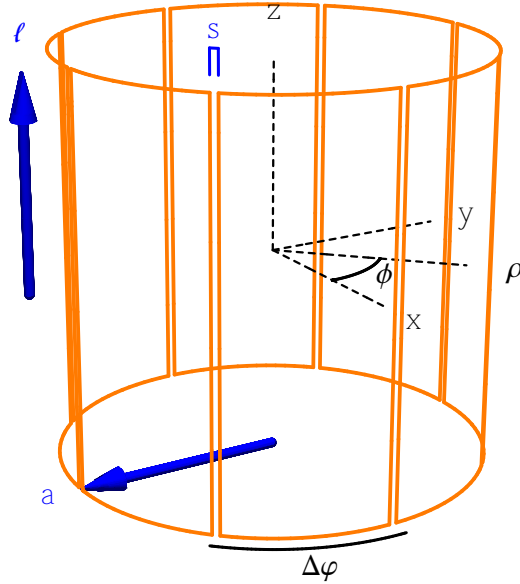


Figure 3: A model of the birdcage-like coil. It is comprised of eight individual saddle coil elements, each of length  $2\ell$  and wound on radius  $a$ . The arc length spacing between segments is given as  $s$ , and  $\Delta\varphi$  is the angle subtended by the sum of  $s$  and a single coil segment. The orientation of cartesian coordinates  $(x, y, z)$  and cylindrical coordinates  $(\rho, \phi, z)$  are shown in relation to the coil.

For the purpose of conforming with the constructed prototype coil, I have chosen here to make  $N = 8$ . Figure 4 depicts plots of  $\sin(n\phi)$  and  $\cos(n\phi)$  over  $2\pi$  for  $n = 1, 2, 3, 4$ . It also shows dots spaced at  $\pi/4$  intervals. This plot represents the birdcage-like approximation for 8 segments. The x-axis represents the circumference of cylindrical distribution. The dots are the points at which adjacent segments meet and where  $\sin(n\phi)$  and  $\cos(n\phi)$  is approximated by discrete values. There are  $N$  points of discrete  $\sin(n\phi)$  current for an  $N$  segment coil. For  $\sin(1\phi)$ , each period of sin is approximated by 8 points. For  $\sin(2\phi)$  and  $\sin(3\phi)$ ,  $\sin(4\phi)$ , each period of sin is approximated by 4,  $8/3$ , and 2 points, respectively. As  $n$  increases, the number of points available to approximate the  $\sin(n\phi)$  distribution decreases for fixed  $N$ . There is an upper limit of  $n = N/2$  modes for an  $N$  segment coil. This can be seen from the Nyquist sampling theorem [6]: a harmonic function of period  $W$  can be determined by points evenly spaced a distance no more than  $1/(2W)$ . In our case, this theorem implies

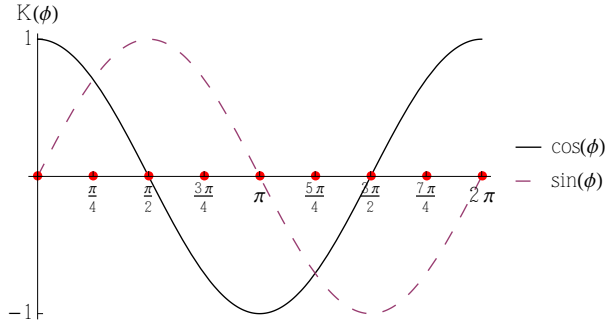
that  $\sin(n\phi)$  can be determined over the range  $\phi = 0 \rightarrow 2\pi$  by no less than  $N = 2n$  evenly spaced points. For  $N = 8$  segments, the highest possible mode that can be approximated is  $n = 4$ , and is visualized in Figure 4d. Any higher modes would be undersampled for such a coil and this would lead to aliasing.

It is desirable to derive a formula for the current in each segment necessary to produce some arbitrary transverse uniform field or gradient field, so that the birdcage-like coil can be put into practice. We start with an expression for the currents flowing axially along a cylindrical surface at the  $N$  discrete points where adjacent segments meet:

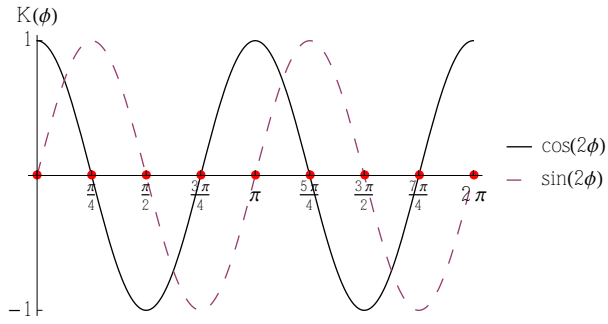
$$I_j = \int_{\varphi_j - \Delta\varphi/2}^{\varphi_j + \Delta\varphi/2} K \sin(n\phi) a d\phi = I \sin(n\varphi_j), \quad (4)$$

where  $j = 1, 2, \dots, N$ ,  $I = aK \frac{2}{n} \sin(n\frac{\pi}{N})$ ,  $\Delta\varphi = \frac{2\pi}{N}$  is the angle between axial line currents as seen in Figure 3, and  $\varphi_j = \Delta\varphi(j - 1)$  is the angular position of each successive line current. This current distribution is proportional to  $\sin(n\phi)$ , and it allows us to obtain  $\mathbf{B}$  from Equation 2.

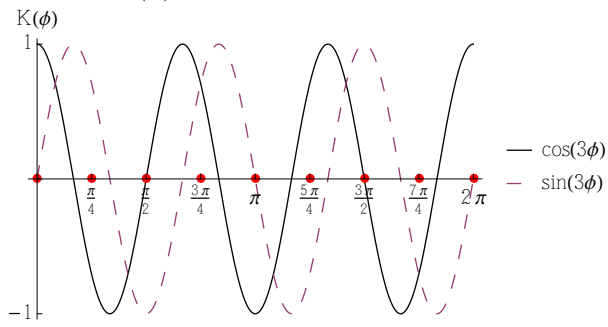
Now, consider the direction of  $\mathbf{B}$  points along the positive x-axis, corresponding to  $\phi = 0$ . We can solve Equation 4 and then find the segment currents that give rise to  $I_j$ . The procedure I followed to find segment currents was to start with the largest axial current and assume its adjacent segments each produce half of that axial current. From there I moved successively along the segments, assigning them current values that add up to their adjacent axial values. A more systematic way would be to solve the currents as a system of  $N$  equations. The solution for  $n = 1$  is shown pictorially in Figure 5, where the dots, as in Figure 4, correspond to the azimuthal location of the wires.



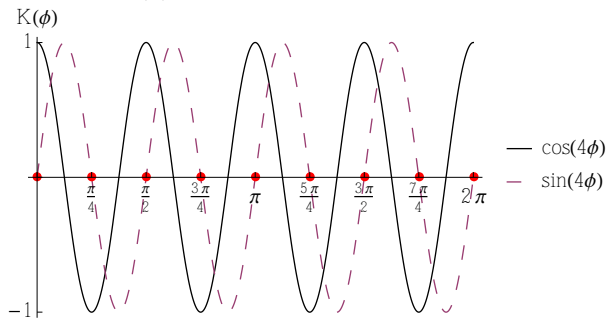
(a)  $n = 1$



(b)  $n = 2$



(c)  $n = 3$



(d)  $n = 4$

Figure 4: Plots of  $\sin(n\phi)$  and  $\cos(n\phi)$  for  $n = 1, 2, 3, 4$  along with dots representing positions of discrete current.

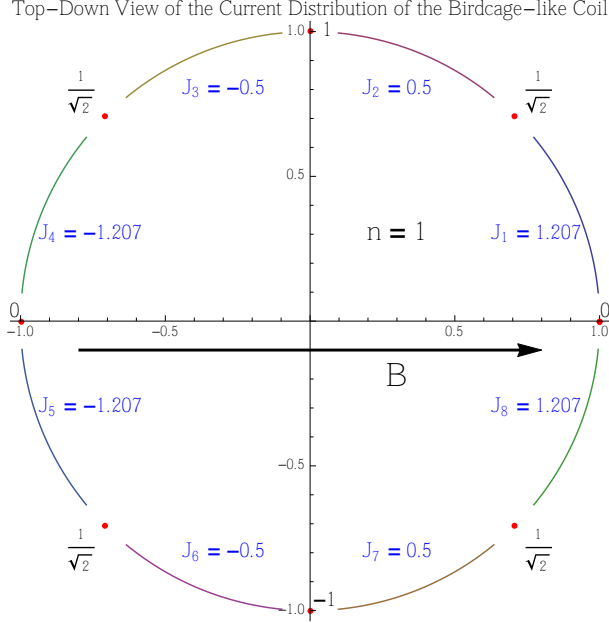


Figure 5: Individual segment current distribution, along with the  $\sin(1\phi)$  discrete current distribution, for  $N = 8$ . The values along the circumference at angles  $\varphi_1$  through  $\varphi_8$  are the currents  $\sin(1\varphi_j)$ . The end ring currents,  $J_1$  through  $J_8$ , are the same as the segment currents. Positive current flows clockwise. Note that adjacent axial segment rung currents sum to give the correct  $\sin(1\varphi_j)$  current where the end rings meet. The angle describing the azimuthal orientation of the field is  $\varphi = 0$  (see Equation 5).

It is a simple procedure to determine segment currents when  $\mathbf{B}$  points towards  $\varphi_j$ . In this case, the currents are merely permutations of the current configuration that arises for  $\mathbf{B}$  pointing along  $\hat{\mathbf{x}}$ , which corresponds with  $\varphi_1$  (i.e. the current configuration seen in Figure 5). To obtain an equation for the segment currents that generate arbitrary transverse  $\mathbf{B}$ , we must add a linear combination of independent current configurations that give rise to orthogonal  $\mathbf{B}$  fields; for example, along  $\hat{\mathbf{x}}$  and  $\hat{\mathbf{y}}$ . It turns out that independent configurations for arbitrary mode  $n$  generate fields that are oriented at angles  $\phi_0$  and  $(\phi_0 + \frac{\pi}{2n})$  where  $\phi_0$  is an arbitrary angle. This can be visualized with Figures 1 and 2. We know that  $\sin(n\phi)$  and  $\cos(n\phi)$  are linearly independent of each other. Between  $\sin(n\phi)$  and  $\cos(n\phi)$  in Figures 1 and 2, magnetic poles are separated by an angle of  $\frac{\pi}{2n}$ . Therefore, linearly independent current configurations will be rotations of that same angle  $\frac{\pi}{2n}$ . I have taken  $\phi_0$  to be 0 for my calculations, as is seen in Figure 5.

Finally, the segment current configurations can be written for  $n = 1, 2, \dots, \frac{N}{2}$ . For  $n = 1$

we have,

$$2aK \sin\left(\frac{\pi}{8}\right) \begin{pmatrix} \left(\frac{1}{2} + \frac{1}{\sqrt{2}}\right) & \frac{1}{2} \\ \frac{1}{2} & \left(\frac{1}{2} + \frac{1}{\sqrt{2}}\right) \\ -\frac{1}{2} & \left(\frac{1}{2} + \frac{1}{\sqrt{2}}\right) \\ -\left(\frac{1}{2} + \frac{1}{\sqrt{2}}\right) & \frac{1}{2} \\ -\left(\frac{1}{2} + \frac{1}{\sqrt{2}}\right) & -\frac{1}{2} \\ -\frac{1}{2} & -\left(\frac{1}{2} + \frac{1}{\sqrt{2}}\right) \\ \frac{1}{2} & -\left(\frac{1}{2} + \frac{1}{\sqrt{2}}\right) \\ \left(\frac{1}{2} + \frac{1}{\sqrt{2}}\right) & -\frac{1}{2} \end{pmatrix} \begin{pmatrix} \cos(\varphi) \\ \sin(\varphi) \end{pmatrix} = \begin{pmatrix} J_1 \\ J_2 \\ J_3 \\ J_4 \\ J_5 \\ J_6 \\ J_7 \\ J_8 \end{pmatrix}. \quad (5)$$

For  $n = 2$ ,

$$aK \sin\left(\frac{\pi}{4}\right) \begin{pmatrix} \frac{1}{2} & \frac{1}{2} \\ -\frac{1}{2} & \frac{1}{2} \\ -\frac{1}{2} & -\frac{1}{2} \\ \frac{1}{2} & -\frac{1}{2} \\ \frac{1}{2} & \frac{1}{2} \\ -\frac{1}{2} & \frac{1}{2} \\ -\frac{1}{2} & -\frac{1}{2} \\ \frac{1}{2} & -\frac{1}{2} \end{pmatrix} \begin{pmatrix} \cos(2\varphi) \\ \sin(2\varphi) \end{pmatrix} = \begin{pmatrix} J_1 \\ J_2 \\ J_3 \\ J_4 \\ J_5 \\ J_6 \\ J_7 \\ J_8 \end{pmatrix}. \quad (6)$$

For  $n = 3$ ,

$$\frac{2}{3}aK \sin\left(3\frac{\pi}{8}\right) \begin{pmatrix} \left(\frac{1}{\sqrt{2}} - \frac{1}{2}\right) & \frac{1}{2} \\ -\frac{1}{2} & -\left(\frac{1}{\sqrt{2}} - \frac{1}{2}\right) \\ \frac{1}{2} & -\left(\frac{1}{\sqrt{2}} - \frac{1}{2}\right) \\ -\left(\frac{1}{\sqrt{2}} - \frac{1}{2}\right) & \frac{1}{2} \\ -\left(\frac{1}{\sqrt{2}} - \frac{1}{2}\right) & -\frac{1}{2} \\ \frac{1}{2} & \left(\frac{1}{\sqrt{2}} - \frac{1}{2}\right) \\ -\frac{1}{2} & \left(\frac{1}{\sqrt{2}} - \frac{1}{2}\right) \\ \left(\frac{1}{\sqrt{2}} - \frac{1}{2}\right) & -\frac{1}{2} \end{pmatrix} \begin{pmatrix} \cos(3\varphi) \\ \sin(3\varphi) \end{pmatrix} = \begin{pmatrix} J_1 \\ J_2 \\ J_3 \\ J_4 \\ J_5 \\ J_6 \\ J_7 \\ J_8 \end{pmatrix}. \quad (7)$$

For  $n = 4$ ,

$$\frac{1}{2}aK \sin\left(\frac{\pi}{2}\right) \begin{pmatrix} \frac{1}{2} & \frac{1}{2} \\ \frac{1}{2} & -\frac{1}{2} \\ \frac{1}{2} & \frac{1}{2} \\ \frac{1}{2} & -\frac{1}{2} \\ \frac{1}{2} & \frac{1}{2} \\ \frac{1}{2} & -\frac{1}{2} \\ \frac{1}{2} & \frac{1}{2} \\ \frac{1}{2} & -\frac{1}{2} \end{pmatrix} \begin{pmatrix} \cos(4\varphi) \\ \sin(4\varphi) \end{pmatrix} = \begin{pmatrix} J_1 \\ J_2 \\ J_3 \\ J_4 \\ J_5 \\ J_6 \\ J_7 \\ J_8 \end{pmatrix}. \quad (8)$$

In all the above I have chosen  $N = 8$ . The segment currents are labeled  $J_1$  through  $J_8$ . Note that  $\varphi$  is the angle describing the azimuthal orientation of  $\mathbf{B}$  within the coil. I have taken the orientation of the fields for  $\sin(n\phi)$  (Figure 1) to be  $\varphi = 0$ . For the  $n = 1$  mode,  $\varphi$  describes the direction of  $\mathbf{B}$ . Using Equations 5 to 8, uniform and gradient fields up to mode  $n = 4$  can be generated in some arbitrary transverse orientation.

## 2.3 Contour plots of the birdcage-like model magnetic field

A computer model of the birdcage-like coil was created for the purpose of investigating its properties. Using the computer model of the birdcage-like coil (see Appendix B) and its generated magnetic field, contour plots of said field were created. The idea is to compare the magnetic field due to the birdcage-like coil as it is split up into various number of segments. See Figure 6 for the contour plots and their orientation in the  $z = 0$  plane. Segment currents flow so that the generated field points along the positive horizontal direction,  $\hat{\mathbf{x}}$ .

The value plotted is the percent difference of the field compared to the isocenter<sup>1</sup> which is at the center of each plot. Only  $\mathbf{B}_x$  is plotted. Especially with these plots being of ideal computer models, the other two components of  $\mathbf{B}$  are negligible in the central region near the isocenter.

Contours go negative as they become darker shades of purple, and they go positive as they become lighter shades towards yellow. This corresponds to darker contours being smaller than the isocenter field, while lighter contours being larger than the isocenter field.

As expected, homogeneity within the coil increases with  $N$ . The spacing between contours changes markedly from 10% to 0.1% to 100 ppm for  $N = 4, 12, 32$ , respectively. This is due to the ideal  $\sin(n\phi)$  surface current distribution being more closely approximated for greater  $N$ . The magnetic field approaches perfect homogeneity as  $N$  grows.

Because of the way the segment currents sum together when  $N = 4$ , Figure 6a approximates two line currents flowing out of the page at position (0,1) and into the page at (0,-1). The field grows traveling in the direction of (0,1) or (0,-1) and falls off traveling away from those points. In Figure 6b, the segment rungs approximate 10 line currents flowing either in or out of the page on the cylindrical surface. With more line currents approximating the appropriate surface current, the homogeneity covers a more circular region within the coil in the  $z = 0$  plane. Finally, in Figure 6c there are 30 approximated line currents on

---

<sup>1</sup>The isocenter is the origin of the coordinate system in Figure 3, the point at the axial and radial centre of the coil.

the cylindrical surface. The homogeneity is now more evenly distributed. Contour lines are smoother within the coil.

### 3 Prototype design and characterization

Herein I will discuss notable features of the birdcage-like coil, the construction and specifications of the built prototype coil, and the methods used in testing the built prototype coil. The prototype coil was characterized by measuring its self-resonance, inductance, resistance, and homogeneity.

#### 3.1 Features of the birdcage-like coil

There are several notable features of the birdcage-like coil that are especially convenient for construction and operation.

1. This design is simply a collection of saddle coils, making it is an easy design to build on the surface of a cylinder. Wire is wound so that it either follows an axial path, or an angular path. This makes for simple construction. It also can be a very sturdy design with the cylindrical shell holding the coil rigidly in place. It is possible that an appropriate cylindrical shell can be bought off the shelf.
2. It is convenient to have uniform and gradient fields up to the  $N/2$  mode produced by the same coils. Certain other uniform field coil designs do not produce gradient fields.
3. In Equation 5, we see that certain rows of the matrix are linearly dependent. For  $J_1$  to  $J_4$ ,  $J_i = -J_{i+4}$ . This means that opposing segments ( $J_i$  and  $J_{i+4}$ ) can be connected in series. This allows for  $N/2 = 4$  power supplies to control the field of the  $n = 1$  mode. From Equations 6 to 8 we see that for  $n = 2$ , opposing segments run the same current which means they can be connected in series opposition. This also allows for four power supplies to be used. For  $n = 3$ , opposing segments run negative currents of

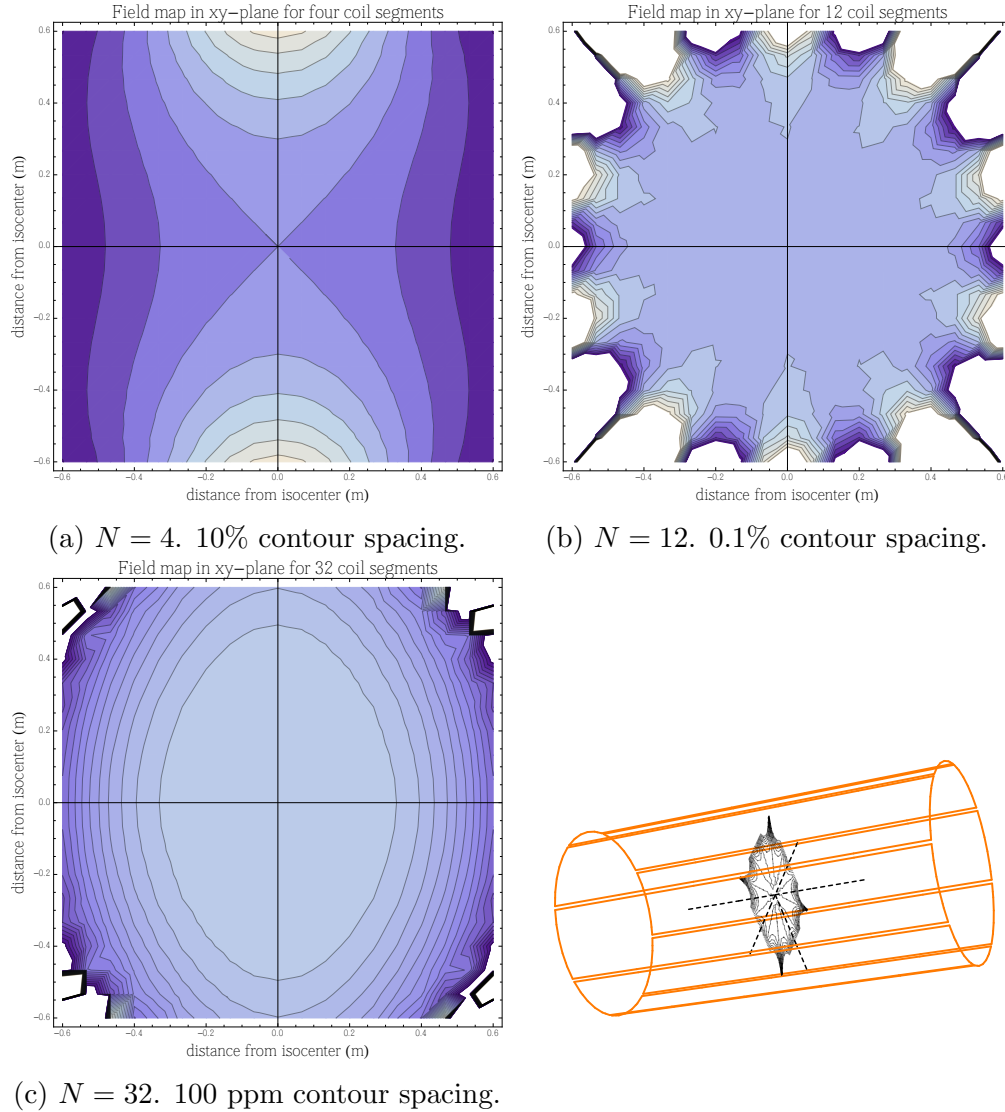


Figure 6: Contour plots of  $B_x$  for varying  $N$  (4, 12, and 32) in the  $n = 1$  mode. Plotted over  $0.6 \cdot$ radius of the coil (the radius  $a$  is 1 m). End segments of the model coil are approximated by five discrete chunks. Length is  $4 \cdot$ radius. Contour spacing decreases as  $N$  increases. The contour plot for 12 segments situated within the model coil it corresponds with (bottom right). Note that the proportions of this coil are to scale.

each other, can be connected in series opposition, so they can operate with four power supplies. For  $n = 4$ , every second segment runs the same current, can be connected in series opposition, so they can operate with two power supplies. However, if one would like to transition from one mode to another on the fly, all segments must run independently. This is due to the fact that opposing segments must run the same current in one mode, but negative current in another.

### 3.2 Prototype construction

In order to investigate the birdcage-like coil for its homogeneity and as a possible active magnetic shield, a prototype was constructed for testing. The number of segments for the coil was chosen to be eight. This decision was primarily out of concern for the number of power supplies necessary to run segment currents.

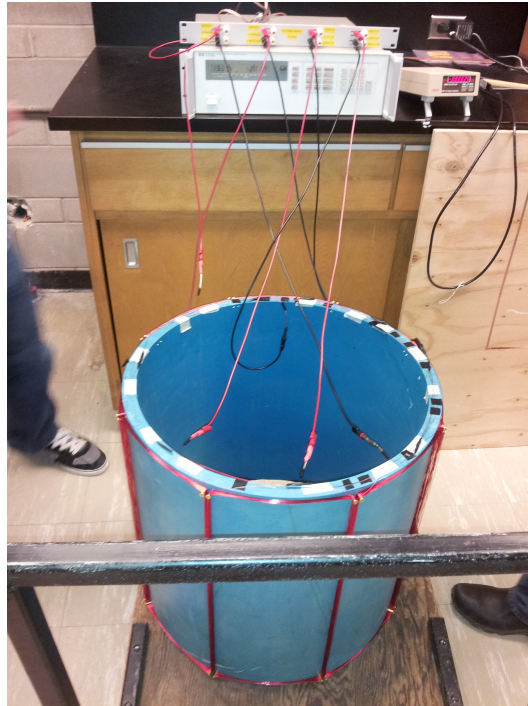


Figure 7: The birdcage-like prototype coil constructed for testing, along with the four output power supply connected to the coil.  $N = 8$ . Opposing segments are soldered together in series.

The coil was built on a hollow cylindrical water pipe made out of some unknown type

of plastic. The plan for construction was to wrap wire on the outside surface to form each segment. Four screws were drilled into the outer surface of the pipe for each segment as posts on which the wire would be wound. It did not matter whether the screws were electrically conductive because there was no way for them to make a short circuit with anything. However, sturdy screws are desirable because a number of them broke while being drilled into the plastic. See Figure 7 for the built prototype coil connected to a multi-output power supply.

Specification of the prototype coil are given in Table 1:

Table 1: Properties and specifications of the prototype coil itself

Specification	Value
Length	$(53.6 \pm 0.3)$ (cm)
Radius	$(56.0 \pm 0.1)$ (cm)
Segment spacing	$(5.5 \pm 0.2)$ (mm)
Wire used per segment	25 turns of 26 gauge copper wire
Isocenter magnetic field produced	$(75.6 \pm 0.8)$ $\mu\text{T}^2$

Assuming  $N = 8$ , the  $n = 1$  mode allows opposing segments to be connected. For the prototype coil, opposing segments were connected in series with one of the segments having its polarity reversed. Hence, four power supplies can be used as opposed to eight.

Opposing segments were connected by a wire that runs along the top of the circumference of the cylinder in Figure 7 (the tape securing these wires to the circumference is visible). The two ends of each connected pair segment were brought together by running another wire along the circumference of the cylinder, on top of the first wire. The field generated by these two circumferential wires is negligible because of their proximity and opposing currents.

The power supply used was an Agilent 6624A DC four-output power supply. The outputs

---

<sup>2</sup>The field displayed is  $\mathbf{B}_x$ , which is the dominant field in the central region of the coil. The magnetic field produced is dependent on the scaling of the current in the coil segments. Consequently, it makes sense to use a field-per-unit-current of the coil when comparing to Earth’s field. The prototype field produced can be thought of as field-per-unit-current ( $\mu\text{T}/\text{A}$ ) where the current referenced is the maximum current along the cylindrical surface of the ideal axial distribution. From Equation 5,  $I = 2aK \sin(\pi/8)$  was set to one. So, the field produced is the isocenter field for  $(1 \cdot \sin(\phi))\text{A}$  axial current.

were restricted to 0 to 20 V, and 0 to 2 A.

The total magnitude of Earth’s field was roughly 44  $\mu\text{T}$  in the region of the prototype while testing occurred. The prototype produced a magnetic field-per-Ampere<sup>2</sup> greater than Earth’s field. This is nice because a field large enough to cancel out Earth’s field is generated at relatively low current, and consequently low power dissipation. There were no problems with heat dissipation in the coil while testing.

### 3.3 Methods

What follows are the methods used in characterizing the constructed prototype coil. Self-resonance, inductance, resistance, and homogeneity were measured.

#### 3.3.1 Self-resonance measurement

The birdcage segments have inherent inductance and self-capacitance, which means that they are RLC circuits when running AC current and will self-resonate at certain frequencies. The RLC circuit impedance is given as,

$$Z = \sqrt{R^2 + (\chi_L - \chi_C)^2}, \quad (9)$$

where  $\chi_L = \omega L$  and  $\chi_C = \frac{1}{\omega C}$ . When the frequency of the coil is greater than resonance,  $\chi_L$  dominates and the coil acts more as a capacitor. The magnetic field produced by the coil above resonance will not behave as expected. It is therefore important to operate the coil at frequencies safely below any coil self-resonance so that the generated field behaves properly.

It is also valuable to measure the self-resonant frequencies of the birdcage-like coil because the coil will not behave as desired at resonance. Currents in the coil will rise at resonance, and because precise currents must be maintain in each coil segment, the magnetic field generated will change and homogeneity will be poorer.

For this measurement, opposing segments had been severed, so self-resonance was mea-

sured for a single coil segment. Also, coil segments were kept as an open circuit. With the prototype oriented so that its axis pointed vertically, a transmit coil was placed centered just under a segment. A receive coil was placed just above the same segment, on an axis perpendicular to that of the transmit coil. The transmit coil was connected to a function generator producing a sine wave. The receive coil was connected to an oscilloscope with its signal displayed. The frequency of the function generator’s sine wave was swept through 1 kHz up to 10 MHz. Any spike in the magnitude of the receive loop’s signal was viewed on the oscilloscope and was recorded as a self-resonance. See Figure 8 for the circuit diagram of the coils set up in order to find self-resonances.

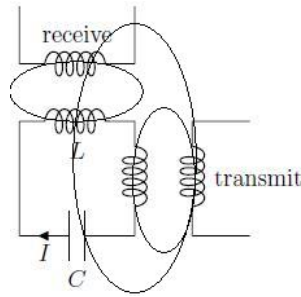


Figure 8: The circuit diagram of the apparatus for the self-resonance measurement, along with magnetic field lines due to the driven transmit coil. The transmit coil is driven in order to produce a magnetic field that couples with the birdcage segment. The birdcage segment then couples with the receive coil, and its signal is measured. The loops represent magnetic field lines. The smaller field line loops are coupled. Note that when the transmit and receive coils are perpendicular to each other, shared magnetic flux is smaller (represented by the large magnetic loop not passing through the core of receive coil inductor).

The two transmit and receive coils were later brought near each other with nothing else nearby to couple with. The same procedure of sweeping through the function generator’s frequency was performed to check whether any of the measured self-resonant frequencies were due to either of the transmit/receive coils themselves.

### 3.3.2 Resistance and inductance measurements

Resistance and inductance were measured by a four-point measurement using a lock-in amplifier. The resistance and inductance are valuable to determine because these quantities are

due to geometry/conductor material and they define a coil. They also serve as a check of a coil's continuity. The resistance and inductance of a coil are dependent on the number of turns of wire and so they can be used to verify the number of turns in a coil.

Oposing segments were connected for this measurement, and values were recorded for each of the four opposing segment pairs. See Figure 9 for the circuit diagram of the setup for this measurement.

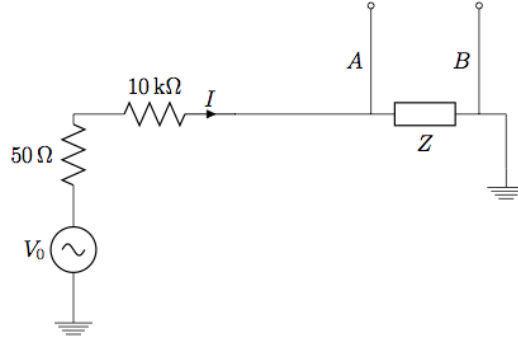


Figure 9: The circuit diagram of the setup for the resistance and inductance measurement

Here  $V_0 = 1.000$  is the applied RMS voltage of the lock-in amplifier, the  $50 \Omega$  resistance is internal to the lock-in amplifier,  $Z$  is the measured value of the segment pair defined in Equation 10, and  $A$  and  $B$  are where the lock-in amplifier measures the voltage drop of the coil segment. The segment pair was connected to the 'sine out' of the lock-in amplifier with a  $10 \text{ k}\Omega$  resistor between them. The equation for  $Z$  is as follows,

$$Z = R + i\omega L = \frac{X}{I} + i\frac{Y}{I}. \quad (10)$$

Here  $R$ , and  $L$  are coil resistance and inductance,  $\omega$  is frequency,  $I$  is current, and  $X$  and  $Y$  are the Channel 1 and Channel 2 RMS voltage outputs. The phase of the lock-in amplifier was  $0.00$  degrees, and frequency  $f = 1599.5 = 10050/(2\pi)$  Hz. The value of  $10050$  was roughly the resistance of the added resistor and internal lock-in amplifier resistance. The measured value of this added resistance was  $R_{drop} = 10180 \Omega$ . The lock-in amplifier measures voltage directly, but we want  $R$  and  $L$ . After manipulation, we end up with equations for  $R$

and  $L$ ;

$$R = \frac{X}{V_0/R_{drop}},$$
$$L = \frac{Y}{V_0 \cdot 2\pi \cdot f/R_{drop}}.$$

The resistance due to the two wires connecting opposing segments was subtracted from the resistance data. The measured uncertainty was taken to be the error due to fluctuations in the lock-in amplifier output.

### 3.3.3 Field mapping along the $x$ - and $y$ -axes

A simple field mapping test was performed within the coil along the  $x$ - and  $y$ -axes in the  $z = 0$  plane (axial central plane). The coil was oriented so that the axial direction was vertical. Equation 5 was used to generate a homogeneous field for  $\varphi = 0$  (along positive  $x$ -axis). The coil was placed as far as possible from any magnets and from its power supply. A three-axis fluxgate magnetometer was used for measuring the field. The fluxgate was mounted on a ruler such that its internal sensors would lie as close as possible to the  $z = 0$  plane (the three sensors are separated a small distance from each other in the  $z$ -direction) when the ruler was held vertically and rested on the surface the coil was placed on. All that was left to do was translate the fluxgate along each axis and record data at regular intervals. However, the most crucial part of measurement was to assure that the orientation of the fluxgate remained constant while translating along an axis.

To keep the fluxgate orientation constant, two feet were attached to the bottom of the ruler to keep the orientation fixed in one direction. To measure position along the axis and help fix orientation, a ruler was attached on top of the coil along the axis of measurement (but offset just enough so that the vertical ruler holding the fluxgate could rest on the horizontal ruler and lie both vertically and perpendicular to the axis of measurement). Lastly, two lines were drawn on the surface the coil rested on, along the  $x$ - and  $y$ -axes. The bottom of the ruler holding the fluxgate was kept aligned with the line drawn along the axis, again to

ensure the orientation of the ruler remained fixed. Figure 10 depicts the apparatus inside the coil for measurement.

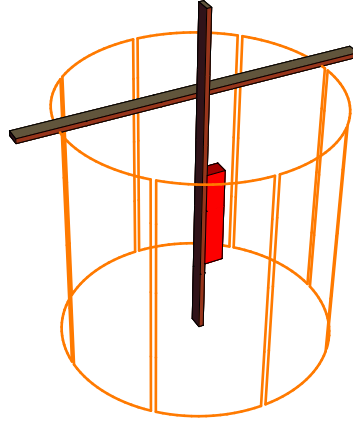


Figure 10: The apparatus used for measuring the magnetic field along the two transverse axes. The red object is the fluxgate which is attached to the ruler oriented vertically.

The field was measured in 1 cm increments from one extreme inside the coil to the other. Each measurement was made twice; once with the coil current on and once with the coil current off. This was done to be able to cancel out Earth's background field. To calculate the uncertainty in the measurement, blind measurements of the field were made five times at two different points along an axis. The fluxgate was positioned at a point along the axis and the field was recorded by another person to eliminate bias in measurement. The fluxgate was removed from its position and then brought back to make the field measurement again. The standard error of these measurements was used as the error. The error was multiplied by two as every point was measured with the coil current both on and off.

## 4 Results

Results of both the prototype tests, and coil/magnetic field modeling are presented in this section.

## 4.1 Prototype self-resonance, resistance, and inductance

The self-resonant frequencies of the prototype coil are given in Table 2. The self-resonant frequencies of the prototype coil are relatively high. Certain forms of interference, such as lighting and AC power at 60 Hz, will not cause any degree of self-resonance in the coil.

Table 2: The self-resonant frequencies of a single prototype segment. We observed five resonances up to 10 MHz

Self-resonance
(470 $\pm$ 10) kHz
(630 $\pm$ 10) kHz
(690 $\pm$ 10) kHz
(780 $\pm$ 10) kHz
(1060 $\pm$ 10) kHz

The resistance and inductance of opposing pairs of saddle segments are given in Table 3. The percent difference between the highest value of segment resistance and lowest value of segment resistance is 0.6%. As resistance was measured for opposing segment pairs connected together, the resistance of 50 turns of wire were measured at a time. If the windings were off anywhere by one turn, say, a difference of roughly 2% would be expected. A 0.6% difference suggests the winding was done correctly. The measured discrepancy is likely due to segments having slight differences in geometry and differences in winding tension.

Table 3: The four opposing segment pairs were measured for resistance and inductance. Values presented here are the average of each opposing pair. The opposing pairs were connected in series for measurement.

Pair	Resistance ( $\Omega$ )	Inductance (mH)
1	(5.10 $\pm$ 0.01)	(1.509 $\pm$ 0.002)
2	(5.09 $\pm$ 0.01)	(1.559 $\pm$ 0.002)
3	(5.07 $\pm$ 0.01)	(1.529 $\pm$ 0.002)
4	(5.07 $\pm$ 0.01)	(1.530 $\pm$ 0.002)

## 4.2 Field mapping

The  $n = 1$  field generated by the prototype coil was measured along the  $x$ - and  $y$ -axes (Figure 3) within the coil. Appropriate currents were applied to the segments so that the direction of the expected field would be in the  $\hat{x}$  direction. Data was recorded at 1 cm intervals to compose a very simple field map. This data was then compared to the computational model (Figure 11). The computational model treats all 25 turns of wire that comprise a coil segment as one line current.

The plots are normalized with respect to the field at the isocenter. Only the on-axis ( $x$ -axis) directional field is shown. The other transverse directional field and the axial directional field are negligible near the coil center along both the  $x$ - and  $y$ -axes.

The data points are offset to the right relative to the isocenter in both plots of Figure 11. In other words, there are more data points along the model curve to the right of the isocenter than to the left of the isocenter. This is due to the way the apparatus was set up in making measurements. The fluxgate sensor used to measure the magnetic field was attached to one side of a ruler. The point of reference used to determine position along an axis was the edge of the ruler where the fluxgate was secured. The sensor within the fluxgate enclosure was offset to the right from that point of reference (Figure 10 shows the fluxgate secured to the side of the ruler where the point of reference is located). Hence, all the data is shifted to the right of center.

Data fitting was performed to determine the isocenter according to the data set. This was done because the isocenter was not measured independently. It was necessary to find an isocenter of the data set so that the data could be matched up against the computer model along the horizontal axis. The modeled field is ideal so its isocenter is known exactly. Therefore, the Chi-squared test was used to compare the data against the computer model as the data was shifted horizontally against the model. About 93% of the data points are within error of the model magnetic field. The isocenter of the data fits well with the isocenter of the model to get this agreement.

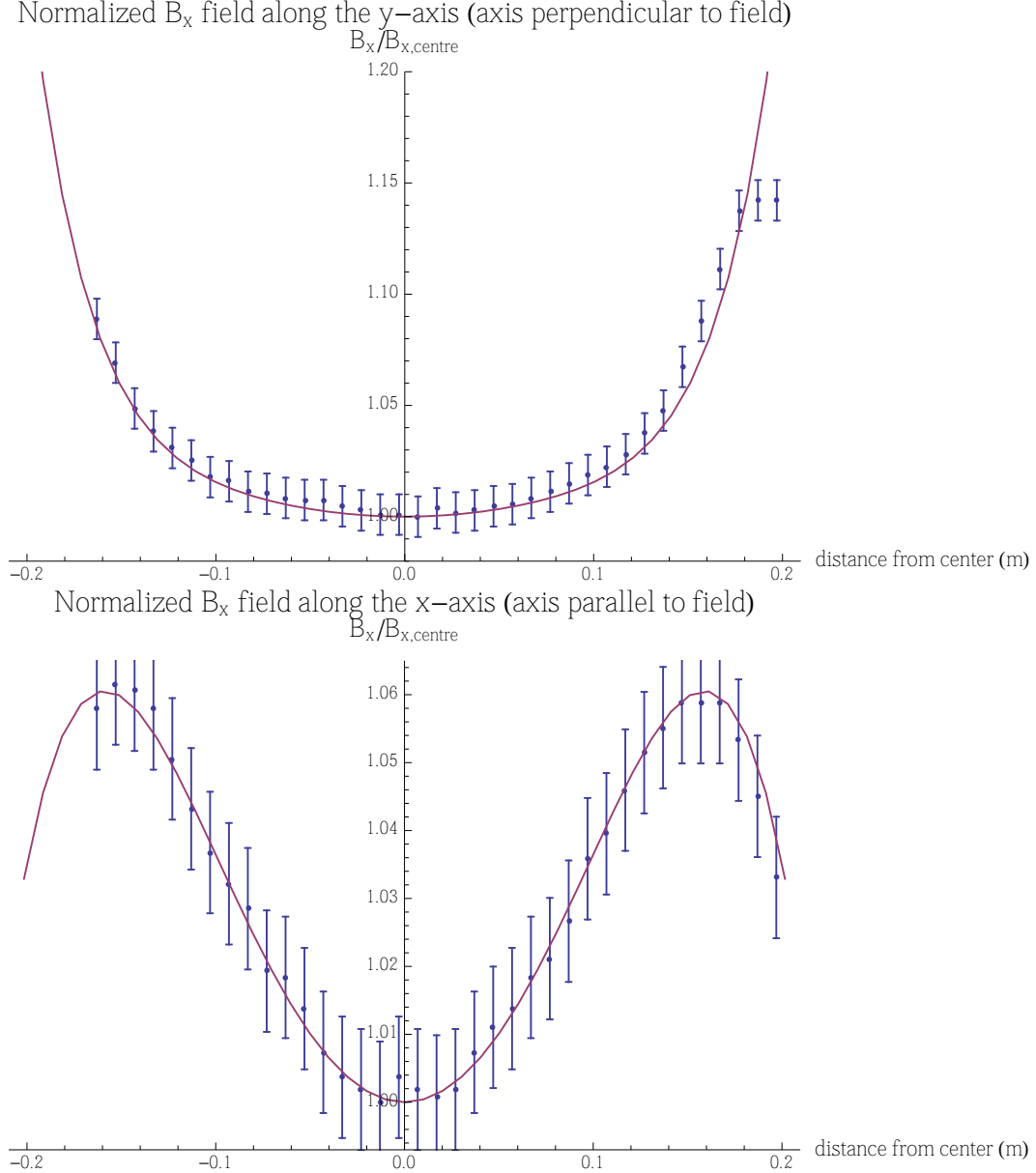


Figure 11: Comparing the  $n = 1$  measured prototype field to the numerical model field: along  $y$ -axis (above), along  $x$ -axis (below). The continuous curve is the field of the numerical model. The center of the horizontal axis is the coil's isocenter. The coil radius is 0.28 m along the horizontal axis. The isocenter field  $B_{x,centre}$  was taken to be the smallest value of each data set.

The curve of  $B_x$  along the  $y$ -axis in Figure 11 is increasing. At  $\pm a$  along this axis there are two rungs of current normalized to  $\pm 1$  (positive and negative directions, respectively). By the right-handed rule, the field due to these two rungs points in the direction of the expected field,  $\hat{x}$ . From Equation 17, the field due to one of these rungs goes as  $1/r^2$ . Consequently,

the field increases as we approach  $\pm a$ . In a similar way, the curve of  $B_x$  along the  $x$ -axis in Figure 11 is decreasing after it reaches a local maximum. There are two rungs of zero current at  $\pm a$  on this axis. The magnetic field will ultimately decrease as we approach these two rungs and move away from the  $\pm 1$  current rungs.

The magnetic field numerical model of the birdcage-like coil is dependent on three parameters (aside from magnitude, which can be ignored if the field is normalized). These parameters can be seen in Figure 3 as  $s$ ,  $a$ , and  $\ell$ . They are the arc length between segments  $s$ ; radius  $a$ ; and half-length  $\ell$ . Slight variations in any of these three parameters causes a distortion to the model curves seen in Figure 11. There was some data fitting involved in matching the measured parameters to the model. The parameters  $s$ ,  $a$ , and  $\ell$  were measured at numerous places on the prototype to obtain a maximum and minimum value for each. The model was then computed while incrementing each parameter within the measured range from minimum to maximum. Values for the parameters were chosen that fit best the experimental data. These values are given in Table 4.

Table 4: The measured range of values for the parameters seen in Figure 3 and Figure 12, as well as the values chosen to fit the modeled magnetic field to experimental data in Figure 11.

	Parameters		
	$s$ (mm)	$a$ (cm)	$\ell$ (cm)
Minimum measured value	5.2	27.35	26.70
Maximum measured value	5.8	28.60	27.00
Mean of measured values	5.5	27.98	26.81
Chosen value	1.0	28.00	26.85

The segment spacing parameter  $s$  was difficult to measure. When the prototype coil was constructed, segments were progressively wound tighter and tighter as the technique for winding was improved. A looser winding leads to wires of adjacent segments approaching each other while a tighter winding keeps adjacent wires apart. This resulted in the segment spacing parameter increasing slightly as successive segments were wound (Figure 12). The space between segments at their lengthwise end (the top of Figure 12) was  $(5.5 \pm 0.2)$  mm.

However, for most of the length of the segments,  $s$  varied from virtually 0 to 2 mm. Note that if the practical minimum and maximum of  $s$  is taken to be 0 and 2, the chosen parameter values in Table 4 are very close to the average of the minimum and maximum.



Figure 12: A close up view of adjacent segments of the prototype coil and the segment spacing  $s$ . Adjacent segments with segment spacing of nearly zero in the middle region (left), and a different set of adjacent segments with a larger segment spacing in the middle region (right). The recorded value of  $s = (5.5 \pm 0.2)$  mm in Table 1 was measured at the top in this figure where the wire wraps around the screws. However, for the majority of the axial length of adjacent segments, the middle region,  $s$  varies from 0 to 2 mm.

The four power supplies that provided currents in generating the  $n = 1$  field were limited in their precision. Two of the supplies provided up to three decimal places of precision. The other two supplies provided two decimal places precision while the currents to be generated by the supplies were on the order of 1 A. The current generated by the power supplies was not always the same as the inputted values which lead to a percent error between the actual current generated and the ideal currents desired. This percent error varied from 0.2% to 2%.

Table 5 gives results for the homogeneity of the prototype magnetic field along the  $x$ - and  $y$ -axes for different fractions of radius. Only the on-axis field is considered. The data points are selected values from both sides of the isocenter seen in Figure 11.

Table 5: Percent difference of the prototype field compared to the isocenter along the two transverse axes. Here  $\hat{x}$  is the on-axis field direction while  $\pm\hat{y}$  is perpendicular to the field.

Fraction of Radius	x-axis	y-axis
$0.05 \pm 0.01$	$(0.05 \pm 0.02)\%$	$(0.2 \pm 0.1)\%$
$0.20 \pm 0.02$	$(1.6 \pm 0.2)\%$	$(0.7 \pm 0.1)\%$
$0.34 \pm 0.01$	$(3.4 \pm 0.2)\%$	$(1.7 \pm 0.1)\%$
$0.59 \pm 0.01$	$(5.84 \pm 0.05)\%$	$(10 \pm 1)\%$

### 4.3 End current discretization

It is possible to approximate the  $\sin(n\phi)$  current distribution with a birdcage-like coil that has straight line end currents as opposed to end currents that are circular arcs along the edge of a cylindrical surface. Such a coil is visualized in Figure 13. There may be certain benefits in using this design to create a homogeneous field. Because the segments in this design are flat, one benefit is that construction of this coil could be a simpler task. Also, it may be easier to build the coil modularly so that each segment is constructed separate from the others. A modularly designed coil could be disassembled for the sake of easier transportation.

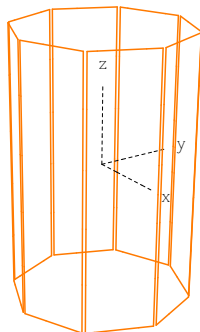


Figure 13: The birdcage-like coil with straight end currents as opposed to curved end currents.  $N = 8$ .

However, the straight end current coil is an approximation of the birdcage-like coil, as it discretizes the circular arc of an end segment into a single straight line chunk. The birdcage-like coil is itself an approximation of the ideal axial current distribution. Consequently, the

straight end current coil may be less homogeneous than the birdcage-like coil. A comparison was made between the curved end segment coil and a coil in which the end segments were discretized into a variable number of straight chunks. See Figure 14 below.

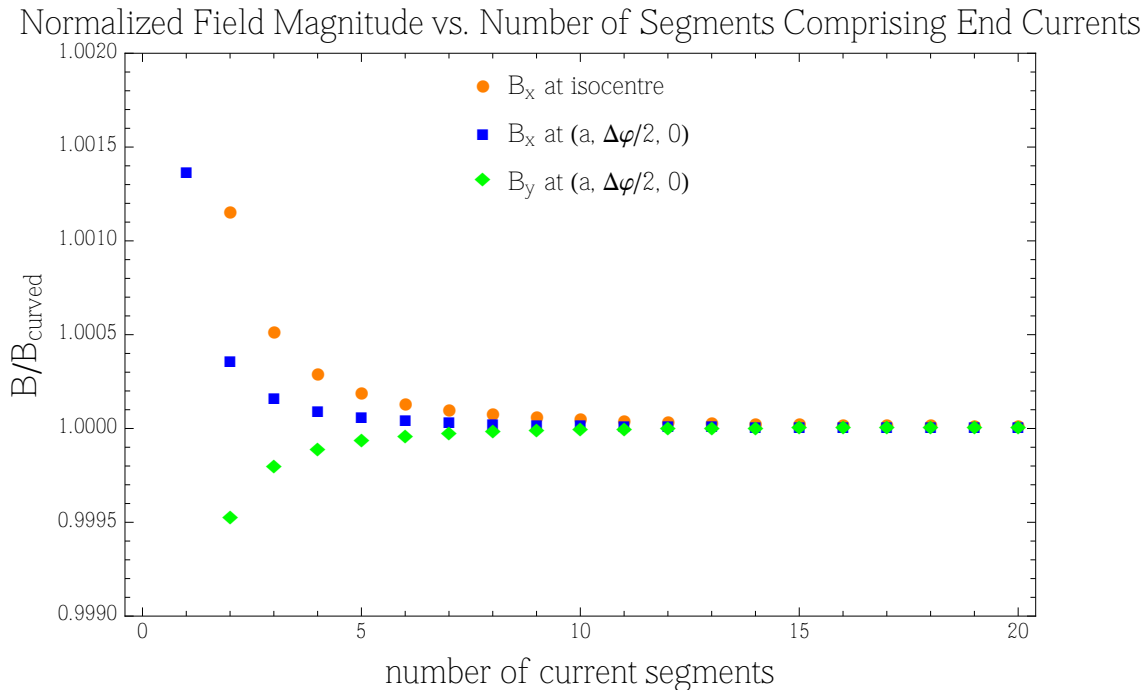


Figure 14: The horizontal axis represents the number of discrete chunks each coil end segment is split up into. The vertical axis is the normalized field. The  $B_x$  and  $B_y$  components of the field at the point  $(a, \Delta\varphi/2, 0)$  are also shown. This extra point on the surface of the cylinder defined by the coil was investigated to check the behaviour of the straight end segment coil outside of the central homogeneous region.  $N = 8$  in this plot.

In Figure 14, two points within the coil are used for comparison; the isocenter and the point in the center of one of the segments with cylindrical coordinates  $(a, \Delta\varphi/2, 0)$ . The coil currents were set up so that the expected field pointed along  $\hat{x}$ . Hence, the field at the isocenter only has a non-negligible  $B_x$ . Because the straight end current coil and the curved end current coil only produce an approximation of a  $\mathbf{B} = B\hat{x}$  field, non-negligible off-axis components of the field arise as we travel towards the surface  $\rho = a$ . A point on the surface  $\rho = a$  will have a non-negligible  $B_y$ . For the  $z = 0$  plane,  $B_z$  is still negligible. Therefore, Figure 14 has one curve for the  $B_x$  at the isocenter, and two curves for the  $B_x$  and  $B_y$  at the point  $(a, \Delta\varphi/2, 0)$ .

Each curve in the figure is normalized with respect to  $\mathbf{B}$  due to the curved end segment coil, at its particular point within the coil. The coil with a single straight current connecting the two segment rungs, represented by  $x = 1$  on the plot, is not actually depicted in the figure. The normalized field for one end current chunk coil is 1.00454 at the isocenter.

We see that  $\mathbf{B}$  converges to the curved end segment value as the number of end segment chunks increases. Not only do the calculations of the field converge, but they converges rather quickly. When the end segments are discretized into ten chunks, the agreement of both points within the coil is smaller than 100 ppm. This is significant because it means that the birdcage-like coil can safely be modeled by a coil with discretized end currents. For the field modeling I have done, I was safe to split end segments into ten chunks or possibly even less. Computation time is increased when modeling curves by many chunks, but this extra computation is unnecessary in our case.

The curved end segment coil used for this comparison is actually a discretized end segment coil with each segment made up of 100 straight chunks. A circular arc of angle  $\Delta\varphi = \pi/4$  split up into 100 straight chunks is a close approximation to the circular arc. For our purposes, the difference between the field produced by these two coils is negligible. I used a 100 chunk end segment coil for normalization as opposed to a curved current coil because my code was designed for straight line currents exclusively (Appendix B).

We can deduce that as  $N$  increases, the field generated by the straight end segment coil approaches the field generated by the curved end segment coil. As  $N$  increases, the arc length per segment  $\Delta\varphi$  decreases. The angle subtended by  $\Delta\varphi$  will decrease proportionally. The length of the straight line connecting a circular arc approaches the length of the arc as the angle subtended by the arc decreases. In other words, arc length is given by  $L = r\theta$ . The line connecting the arc has length  $d = \sqrt{\sin^2(\theta) + (1 - \cos^2(\theta))}$ ; as  $\theta \rightarrow 0$ ,  $d \rightarrow L$ . Hence, the field due to a straight end segment coil approaches that of a curved end segment coil as  $\Delta\varphi$  decreases and  $N$  increases.

## 4.4 Searching for optimum parameters

There are two parameters that determine the relative geometry of the birdcage-like coil. They are shown in Figure 3: the arc length between segments  $s$ : and aspect ratio of the coil  $\ell/a$ . In Section 4.2, values for the three parameters  $s$ ,  $a$ , and  $\ell$  were sought. Experimentally, each of those three parameters were independent of each other and it was desirable to determine their values independently. In searching for optimum parameters, there are only two relevant parameters because our concern is homogeneity, which is only dependent on relative geometry. Length and radius are combined to give a dimensionless quantity. Scaling the field's magnitude has no bearing on its homogeneity.

The parameters  $s$  and  $\ell/a$  for the prototype coil were somewhat arbitrarily chosen. Ease of construction with the materials at hand was the sole influence in determining the parameters. However, these two parameters are important factors in how homogeneous the model birdcage-like coil will be. Consequently, it is a good idea to search for optimum parameters for a more homogeneous coil design.

One method of parameter searching is to select individual values of  $s$  and  $\ell/a$  for homogeneity comparison. The idea is to increment the parameters each over their own respective range. At each fixed value of  $s$  and  $\ell/a$ , the field is calculated at many points in some region of interest inside the coil. A fit function is used to produce a marker of homogeneity for comparison. This is done over each parameter's range in two-dimensional parameter space. One point in parameter space will have the best homogeneity, giving an estimate of optimum parameters.

A basic investigation in parameter space for optimum parameters was performed. See Figure 15 below.

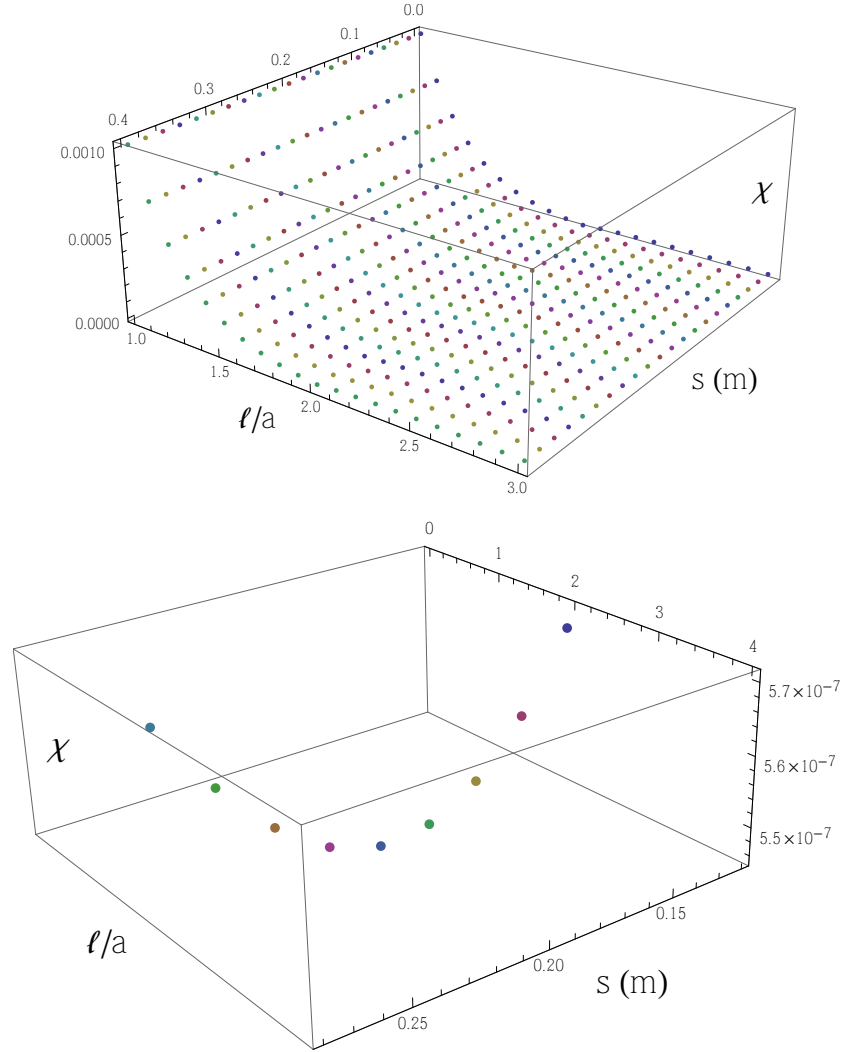


Figure 15: Data points of  $\chi$  which is an RMS variance in the field, in parameter space. A 21x21 grid of values (top) and a close up of the local minimum (bottom). Smaller values of  $\chi$  mean better homogeneity.

The parameter  $s$  was incremented in steps of 2 cm from 0 to 40 cm. The parameter  $\ell/a$  was incremented in steps of 0.1 from 1 to 3. These values make up a grid in parameter space of  $21 \cdot 21 = 441$  data points. In this case,  $s$  was not dimensionless; segment spacing was relative to a radius of 1 m.

Coil currents were set up to flow so that the expected field would be in the  $\hat{x}$  direction. The field was calculated at 1000 points within a spherical region of interest of  $r = 0.1 \cdot a$ . Each cylindrical coordinate was incremented by 10 equally spaced values so that 1000 points

within the volume enclosed by  $r$  were tested. A root-mean-square variance in the field  $\chi$  was then calculated for the 1000 points, comparing them to the isocenter value. This results in a single value for fixed  $s$  and  $\ell/a$ , which is a number assigned to a point in parameter space. A smaller  $\chi$  value corresponds with better homogeneity. Figure 15 consists of these  $\chi$  values in parameter space. The equation for  $\chi$  is as follows,

$$\chi = \frac{1}{B_{x,isocenter}} \sqrt{\frac{\sum_i^N (B_{x,isocenter} - B_{x,i})^2}{N}}, \quad (11)$$

where  $B_{x,i}$  is the x-component of the field at some field point,  $N = 1000$  is the number of field points used, and  $B_{x,isocenter}$  is the x-component of the field at the isocenter.

The local minimum of  $\chi = 5.45 \cdot 10^{-7}$  seen in the bottom plot of Figure 15 has parameter values of  $s = 20$  cm,  $\ell/a = 2$ . However, I must stress that this position in parameter space is merely a local minimum. Although it is possible I found the region where the global minimum resides, I have only searched through part of the useful parameter space. The global minimum where the best homogeneity is to be found could be elsewhere. Even within the range of values I tested, I could still zoom in to a smaller region containing what I found to be a local minimum. I could then test homogeneity again while incrementing parameters more finely to obtain a more precise local minimum. Nonetheless, the local minimum I found is surely better than arbitrarily choosing parameter values as was done for the prototype coil.

## 4.5 Comparing the birdcage-like coil to the square Helmholtz coil

A square Helmholtz coil is a coil composed of two square loops oriented in the same plane with side length  $d$  and separated from each other a distance of  $0.5445 \cdot d$ . If currents are applied in the same direction in both loops, this coil produces a homogeneous field in the direction pointing from the centre of one loop to the centre of the other loop, in the central region between the two loops. The field generated by the birdcage-like coil was compared to

the field generated by the square Helmholtz coil. Contour plots of both fields are shown in Figure 16.

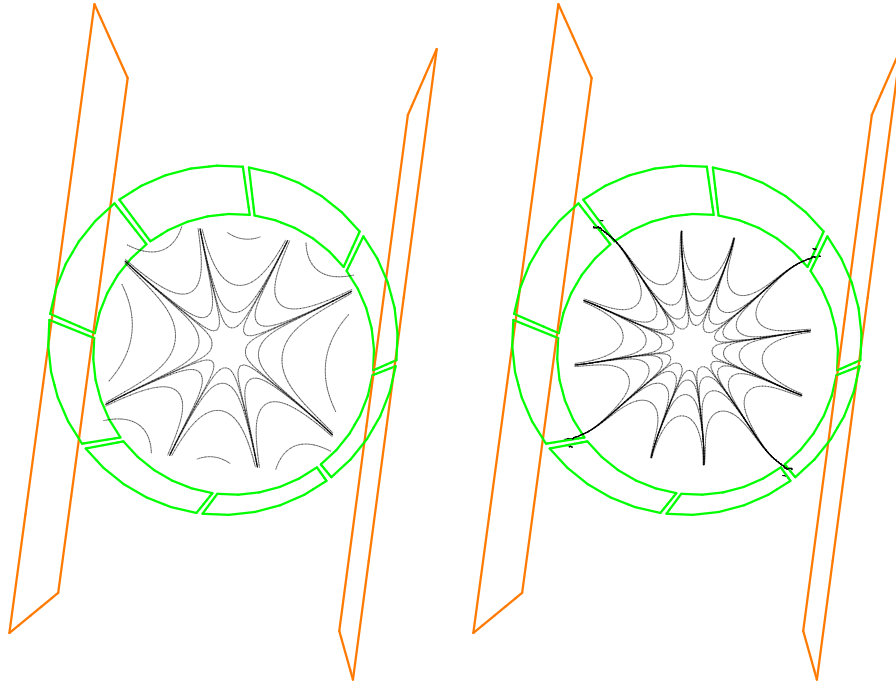


Figure 16: Contour plots of percent difference of  $B_x$  in the  $z = 0$  plane, shown from above. The field generated by the orange square Helmholtz coil (left), and the  $n = 1$  field generated by the green birdcage-like coil (right). The contours moving out from the isocenter are  $\pm(0.001\%, 0.01\%, 0.1\%, 1\%)$ . The parameters of the square Helmholtz coil are: side length  $d$ , and loop spacing of  $0.5445 \cdot d$ . The parameters of the birdcage-like coil are:  $a = 0.5445 \cdot d$ ,  $\ell/a = 2$ ,  $s = 1^\circ$ , and  $N = 8$ . With an aspect ratio for the birdcage-like coil of  $\ell/a = 2$ , its axial length is  $4 \cdot a = 1.089 \cdot d$ .

Coil currents flow in both coils so that the dominant field is  $B_x$ , and only  $B_x$  is plotted. The contours are of percent difference compared to the isocenter field. Moving out radially from the isocenter the contours are either  $0.001\%$ ,  $0.01\%$ ,  $0.1\%$ ,  $1\%$  or  $-0.001\%$ ,  $-0.01\%$ ,  $-0.1\%$ ,  $-1\%$ . The contours alternate azimuthally from positive percent difference to negative percent difference.

It is difficult to compare the field of these two coils directly using some parameter that is fair for comparison. For my comparison, I have chosen to equate the square Helmholtz loop spacing to the birdcage-like cylindrical diameter. These were the parameters that were fixed

in order to compare the generated fields. Some other value can be equated for the sake of comparison, for example, the volume enclosed by each coil.

The square Helmholtz coil provides better homogeneity than the birdcage-like coil in the  $z = 0$  plane in this comparison. The central area within by the  $\pm 0.001\%$  contours is similar for both coils. However, for higher percent differences, the contours of the square Helmholtz field are a larger distance from the isocenter than the same contours of the birdcage-like field. Hence, we see in Figure 16 that the area within the  $\pm 1\%$  contours of the square Helmholtz field is significantly larger than the area within  $\pm 1\%$  contours of the birdcage-like field. Certain parameters of the birdcage-like coil can be varied to increase its homogeneity relative to the square Helmholtz coil. These include the number of segments  $N$  and the fixed parameter used for the purpose comparison.

## 5 Discussion

In Section 2.3, it was shown that orders of magnitude improvement of homogeneity can be achieved by increasing  $N$ . On the other hand, there is a significant trade-off when increasing  $N$  for this achievement in homogeneity. First, there are more discrete values to approximate  $\sin(n\phi)$  by, which increases the current necessary to run the coil. Not only that, but as  $N$  increases there are more adjacent rungs running currents that largely cancel each other out. So, there is more current needed, but also more wasted current needed to increase  $N$ . Of course, the electric power will increase as well. Second, the number of power supplies necessary to run all segments increases with  $N$ . Third, construction of a birdcage-like coil as  $N$  increases will be more challenging and expensive. There are more segments to wind and consequently more wire is needed for the coil. With more coil segments to situate and wind, it is more likely for winding errors and segment positioning errors to build up.

The field mapping discussed in Section 4.2 shows that the homogeneity of the prototype coil is good (Table 5). The uniformity of the prototype field is impressive for the simple

construction method used in building the coil. With more professional and precise techniques of construction, a birdcage-like coil producing better uniformity is entirely feasible.

Also, the values of the parameters  $s$  and  $\ell$  determined through data fitting in Section 4 are very close to the mean of the measured values of those same parameters. The segment spacing parameter does not match up closely with its data fitted value. Although, it does match closely if the effective segment spacing is taken to be somewhere between 0 and 2 mm. This problem is due to the construction of the prototype coil (Figure 12) and can be addressed by either improving the winding technique and increasing tension in the wire, or by modifying the coil design. The coil design could be modified so that the path the wire follows would be more restricted, for example, a channel could be milled in the cylindrical pipe for the wire to be wound in. The closeness of the independent parameter measurements to their value obtained through field mapping suggests that these parameters can be reliably measured by field mapping and subsequent data fitting. The combination of careful field mapping and data fitting was a powerful tool for verifying the coil's properties.

From Section 4.4, the parameters  $s = 20$  cm and  $\ell/a = 2$  for  $a = 1$  m gave the best homogeneity out of the 441 points in parameters space tested. If  $s = 20$  cm,  $s$  spans an angle of roughly  $11.5^\circ$ , which is surprising. Better homogeneity near  $\theta = s/a = 0^\circ$  was expected because that is the exact  $\phi$  position where current rungs are meant to approximate  $\sin(n\phi)$ . Adjacent rungs of current better approximate the discrete  $\sin(n\phi)$  values as they approach each other. It is possible that an ideal segment spacing of roughly  $11.5^\circ$  approximates the current distribution of the birdcage-like coil with  $N \cdot 2 = 16$  segments which leads to improved homogeneity.

Similarly,  $\ell/a = 2$  was surprising as a minimum for homogeneity. Greater values of  $\ell/a$  were expected because the birdcage-like coil is meant to approximate an infinite cylindrical distribution. However, the ideal infinite cylindrical distribution does not include end segments that connect current rungs. It is possible that for  $\ell/a = 2$ , end currents are positioned at a distance from each other such that they cancel each other out more than at other values

of  $\ell/a$ .

## 5.1 Future directions

Although some level of field mapping has been done of the  $n = 1$  field, no mapping or testing has been done for a higher mode field of the prototype. From Equation 5, opposing segments have negative current of each other. For  $n = 2$  and Equation 6, opposing segments have the same current. Because opposite segments run in series and have been connected to each other, some small modifications and soldering would need to be done to reverse the polarity of opposing segments to run the  $n = 2$  mode of the prototype. With the modifications to run opposite segments in series opposition, the mode  $n = 2$  field could be mapped and tested.

In Section 4.2, a uniform  $n = 1$  field was generated and mapped within the prototype. However, the field did not point in the expected direction because Earth's magnetic field was added on to the prototype's field. To deal with this, measurements were made of the background field with no currents running and this was subtracted from field when currents were running. In this way, Earth's field was accounted for when measuring coil homogeneity. A further step in controlling the field within the prototype would be to measure Earth's field and then cancel it out with the coil itself. If a canceling out field is added to the generation of a uniform field, the effect of Earth's field would disappear when creating a field in arbitrary transverse direction.

A further step in controlling the field within the prototype would be to automate the power supplies at a higher level. Currently, to change the magnitude or direction of the desired field inside the prototype, segment current values must be manually calculated and punched in to the power supplies. This makes for a field that changes very slowly when prompted. Computer software could be used to control and change the current generated by the power supplies. Also, Equations 5 to 8 could be written into software so that a computer would do the calculations when changing the field. This would make for a field that could be changed quickly when desired.

Finally, working towards higher levels of automation would culminate in an active feedback loop for active magnetic shielding. Some magnitude and direction of a uniform field would be generated. A sensor would then measure any fluctuation in the field. The sensor would communicate with the computer controlling the coil's power supply. Segment currents would then be automatically adjusted to change the field and counteract the measured fluctuation. At some interval of time later, the sensor would again measure any fluctuation in the field and the loop would repeat.

## 6 Conclusion

Numerous properties of the birdcage-like coil were investigated. It is an appropriate and useful coil design for the purpose of generating a transverse homogeneous field. However, preliminary results suggest that the square Helmholtz coil design has better homogeneity within a comparable central region. The birdcage-like coil is also suitable for use as an active magnetic shield, provided the power supplies controlling it are properly automated. For an eight segment coil, the equations necessary to produce all four modes of the coil are given. A prototype birdcage-like coil was built and tested. The prototype's field was mapped along its transverse axes and its homogeneity agrees within error to the field generated by a computer model.

There is much more that can be done in terms of field mapping both the uniform mode and higher order gradient modes of the prototype coil. Also, higher degrees of control over the current running through the prototype coil can yield a rudimentary active magnetic shield. A carefully built birdcage-like coil may very well be suitable as a transverse active magnetic shield in a neutron EDM experiment.

## References

- [1] V.C.A. Ferraro, *Electromagnetic Theory*, Athlone Press, London, 1954 (fifth impression 1967), pp. 414/15.
- [2] W.R. Smythe, *Static and Dynamic Electricity*, second ed., McGraw-Hill, New York, 1950, pp. 279.
- [3] D.J. Griffiths, *Introduction to Electrodynamics*, third ed., Prentice-Hall, Upper Saddle River, 1999, pp. 215/17.
- [4] J.D. Hanson, S.P. Hirshman, Compact expressions for the Biot-Savart fields of a filamentary segment, *Phys. Plasmas*. **9** (2002) 4410-4412.
- [5] C.P. Bidinosti, I.S. Kravchuk, M.E. Hayden, Active shielding of cylindrical saddle-shaped coil: Application to wire-wound RF coils for very low field NMR and MRI, *J. Magn. Reson.* **177** (2005) 31-43.
- [6] C.E. Shannon, Communication in the presence of noise, *Proc. of the Inst. of Radio Eng.* **37** (1949) 10-21.

## A Supplementary equations for the ideal $B$ field

In general, an infinitely long cylindrical surface current of  $\mathbf{K} = K \sin(n\phi)\hat{\mathbf{z}}$  bound to a surface of radius  $a$  produces a vector potential of [2, 1],

$$\mathbf{A}(\rho, \phi) = \frac{\mu_0 a K \sin(n\phi)}{2n} \hat{\mathbf{z}} \begin{cases} (\rho/a)^n, & \rho < a \\ (a/\rho)^n, & \rho > a \end{cases}. \quad (12)$$

Taking the curl of  $\mathbf{A}$  we obtain an expression for the field  $\mathbf{B}$ ,

$$\mathbf{B}(\rho, \phi) = \frac{-\mu_0 K}{2} \begin{cases} (\rho/a)^{n-1} [\sin(n\phi) \hat{\boldsymbol{\phi}} - \cos(n\phi) \hat{\boldsymbol{\rho}}], & \rho < a \\ (a/\rho)^{n+1} [-\sin(n\phi) \hat{\boldsymbol{\phi}} - \cos(n\phi) \hat{\boldsymbol{\rho}}], & \rho > a \end{cases}. \quad (13)$$

If the surface current is instead chosen to be  $\mathbf{K} = K \cos(n\phi)\hat{\mathbf{z}}$ , the vector potential becomes,

$$\mathbf{A}(\rho, \phi) = \frac{\mu_0 a K \cos(n\phi)}{2n} \hat{\mathbf{z}} \begin{cases} (\rho/a)^n, & \rho < a \\ (a/\rho)^n, & \rho > a \end{cases}. \quad (14)$$

The magnetic field due to Equation 14 is,

$$\mathbf{B}(\rho, \phi) = \frac{-\mu_0 K}{2} \begin{cases} (\rho/a)^{n-1} [\cos(n\phi) \hat{\boldsymbol{\phi}} + \sin(n\phi) \hat{\boldsymbol{\rho}}], & \rho < a \\ (a/\rho)^{n+1} [-\cos(n\phi) \hat{\boldsymbol{\phi}} + \sin(n\phi) \hat{\boldsymbol{\rho}}], & \rho > a \end{cases}. \quad (15)$$

## B Biot-Savart law

In magnetostatics, the Biot-Savart law is an equation that describes the magnetic field generated by a steady current flowing in an arbitrary direction. For a line current the Biot-Savart law can be written as [3],

$$\mathbf{B} = \frac{\mu_0}{2\pi} I \int \frac{d\mathbf{I} \times \hat{\mathbf{r}}}{|\mathbf{r}|^2}, \quad (16)$$

where  $I$  is the value of the current,  $d\mathbf{I}$  is a length element along the direction of the current, and  $\mathbf{r}$  is a vector from the source current element to a field point. The above integral can be difficult to solve for a current flowing in an arbitrary direction. An alternative method to solving such an integral is to treat an arbitrary line current as a collection of discrete straight line chunks. The discrete current chunks line up end to end along the path of the continuous arbitrary current as seen in Figure 17. Discrete current chunks will approximate a curved line current more closely as the number of line segments used to approximate increases.

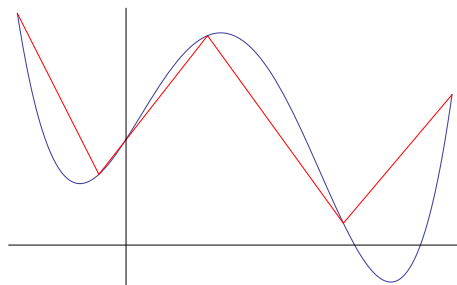


Figure 17: A continuous function approximated by discrete line segments. The function can be thought of as some arbitrary line current of which we want to calculate the field.

A special case of Equation 16 is the field due to a finite straight line. Equation 16 can be rewritten for straight line currents as [4],

$$\mathbf{B} = \frac{\mu_0}{2\pi} I(\hat{\mathbf{e}} \times \mathbf{R}_i) \frac{2L(R_i + R_f)}{R_i R_f} \frac{1}{(R_i + R_f)^2 + L^2}. \quad (17)$$

In the above,  $\mathbf{R}_i$  is the vector from the tail end of the current segment to some field point ( $R_i$  is its magnitude), and  $R_f$  is the distance from the head of the current segment to the field point.  $L$  is the length of the current segment, and  $\hat{\mathbf{e}}$  is the unit vector along the direction the current is flowing. There is no integral in this case of the Biot-Savart law because there is no continuous variable to sum over. Instead,  $\mathbf{B}$  due to an arbitrary current is approximately the sum of Equation 17 over each individual chunk.

Equation 17 is especially well suited to be written as computer code to be numerically solved. It involves addition, multiplication, and a cross product. Performing these calcula-

tions, even for many small current segments, can be a simpler procedure than attempting to tackle Equation 16 directly.

Mathematica code was written to calculate Equation 17 for any distribution of current chunks. With the rewritten Biot-Savart law, all that needs to be specified to calculate  $\mathbf{B}$  is the magnitude of current, positions of the chunk's tail end and head, and the position of a field point. In the code, total  $\mathbf{B}$  is given by summing the field over each chunk whose input are these four values.